Seismic-acoustic energy partitioning during a paroxysmal eruptive phase of Tungurahua volcano, Ecuador

Pablo B. Palacios,[1,2] Mikel Díez,[1] J-Michael Kendall[1] and Heidy M. Mader[1]

[1]*School of Earth Sciences, University of Bristol, Bristol, United Kingdom. E-mail: pablo.palacios@bristol.ac.uk*
[2]*Geophysical Institute of National Polytechnic School, Quito, Ecuador*

SUMMARY

Studies of discrete volcanic explosions, that usually last less than 2 or 3 min, have suggested that the partitioning of seismic-acoustic energy is likely related to a range of physical mechanisms that depend on magma properties and other physical constraints such as the location of the fragmentation surface. In this paper, we explore the energy partition of a paroxysmal eruptive phase of Tungurahua volcano that lasted for over 4 hr, on 2006 July 14–15, using seismic-acoustic information recorded by stations on its flanks (near field). We find evidence of a linear scaling between seismic and acoustic energies, with time-dependent intensities, during the sustained explosive phase of the eruption. Furthermore, we argue that this scaling can be explained by two different processes: (1) the fragmentation region ultimately acts as the common source of energy producing both direct seismic waves, that travel through the volcanic edifice, and direct acoustic waves coming from a disturbed atmosphere above the summit; (2) the coupling of acoustic waves with the ground to cause seismic waves. Both processes are concurrent, however we have found that the first one is dominant for seismic records below 4 Hz. Here we use the linear scaling of intensities to construct seismic and acoustic indices, which, we argue, could be used to track an ongoing eruption. Thus, especially in strong paroxysms that can produce pyroclastic flows, the index correlation and their levels can be used as quantitative monitoring parameters to assess the volcanic hazard in real time. Additionally, we suggest from the linear scaling that the source type for both cases, seismic and acoustic, is dipolar and dominant in the near field.

Key words: Volcano seismology; Acoustic properties; Explosive volcanism.

1 INTRODUCTION

A volcanic eruption disturbs both the ground and the atmosphere, releasing seismic and acoustic energies. If the most intense phase of this process, the paroxysm, involves a magma ejection with a momentum-driven flow, a volcanic jet is formed lasting several minutes to hours, which may be accompanied by massive ash-gas clouds and likely pyroclastic flows (e.g. Cioni *et al.* 2000). At Tungurahua volcano since 2006 the paroxysms have been associated with Vulcanian, sub-Plinian or Plinian eruptions. A better understanding of the relationship between the acoustic and seismic energies radiated by such eruptions will give insights into the dominant physical mechanisms and facilitate a quantitative assessment of volcanic hazards. In this paper we assume that the seismic and acoustic energies are proportional to the kinetic energy released during the eruption fragmentation. The hypothesis that both are linearly proportional is explored in a case study from Tungurahua volcano. This proportionality may be used as a real time indicator of a paroxysmal phase.

Jets have been broadly studied since the middle of 20th century. A first physical model that explains the sound produced by them was proposed by Lighthill (1952, 1954) in which the acoustic sources are instabilities or turbulences carried by the entrainment of one fluid into other. This model was extended by Curle (1955) to include the interaction with solid boundaries. Further measurements and observations of laboratory experiments have shown that fine and large scale structures can act as acoustic sources, that there is directivity of the radiated power, and that the ejection velocity and temperature influence the intensities recorded (Tam 1998; Tam *et al.* 2008). However, none of the current models are capable of explaining all the experimental observations (Viswanathan & Czech 2009) and significant efforts are currently devoted to improving the models (Suzuki 2010), laboratory experiments (Viswanathan & Czech 2009) and the computational simulations (e.g. Lele & Nichols 2014). All these studies are related to the entrainment of one fluid into another, however a volcanic eruption involves additional phenomena that need to be considered, especially in the near field or local region
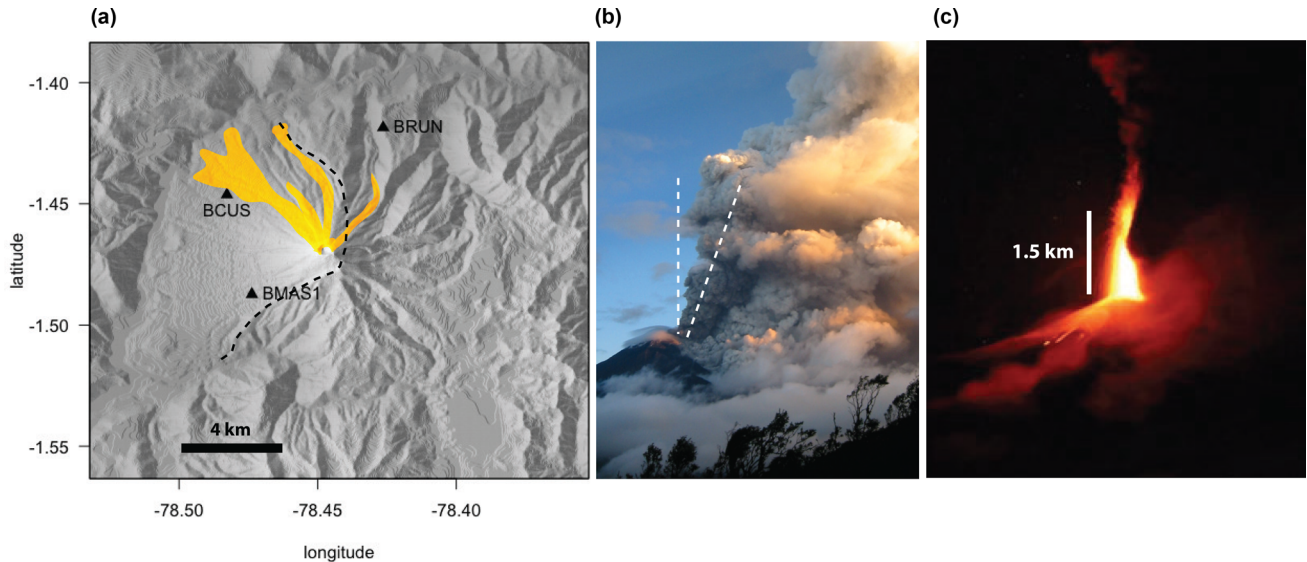
Figure 1. Tungurahua volcano—Ecuador. (a) Seismic-acoustic network (solid triangles) and the approximated region (yellow) affected by pyroclastic flows on 2006 July 14–15. Dashed line: avalanche caldera scar (Hall *et al.* 1999). (b) Jet emission with a deflection angle (defined by the white dashed lines) of the eruption column at 23:18 GMT, July 14. Photo: Santiago Arrais, IGEPN. (c) A 1.5 km height lava fountain at 00:53 GMT, July 15. Photo: Patricio Ramón, IGEPN.

(i.e. less than 15 km around the volcano, Fee & Matoza 2013). In particular:

(i) It is known that acoustic records are affected by the volcanic topography (e.g. Lacanna & Ripepe 2013). Furthermore, in the case of long lasting events, waves reflected off the surrounding mountains are likely mixed with direct waves that arrive at each station (e.g. Yokoo *et al.* 2014).

(ii) Wind conditions and the shape of the volcanic vent may have a significant influence on the radiated acoustic pattern (Kim *et al.* 2012) and on the deflection of the eruption columns (compare fig. 1 in Viswanathan 2011, with our Fig. 1b).

(iii) The interaction of ejected pyroclasts with the atmosphere may provide further acoustic sources (e.g. Woulff & McGetchin 1976; Matoza *et al.* 2013).

(iv) The impact of acoustic waves on the ground causes ground motion (e.g. Ichihara *et al.* 2012) that is superimposed on the seismic waves travelling through the volcanic edifice. This phenomenon was previously observed in the eruption considered in this study in the high frequency range (Palacios *et al.* 2015).

(v) Pyroclastic flows descending on the flanks produce high frequency seismic signals whose recorded intensities depend on the source-station distances (e.g. Kumagai *et al.* 2009; Hall *et al.* 2013).

(vi) The internal volcanic structure and site effects modify seismic waves radiated by the sources.

(vii) A sustained eruption may be characterized by a variable velocity ejection, presence of lightning, strong explosions and seismic events, all representing a complexity that should be taken into account when the records are compared with theoretical models or experimental results.

Some efforts have been made to better understand sustained eruptions, their dynamics and the interactions of magma phases—fluid, solid and gas (e.g. Woods 2010; Jessop & Jellinek 2014). In particular, Woulff & McGetchin (1976) presented power laws, using dimensional analysis, for the radiated-acoustic power of eruptions where their possible sources are monopolar (due to changes in mass flux—explosions), dipolar (fluid–solid interaction) or quadrupolar (fluid–fluid interactions). Matoza *et al.* (2013) modified the quadrupolar

power law to account for the directivity and temperature of the jets. The implication of these concepts, field observations and analyses of far-field infrasound records on Tungurahua, including the case here studied and other volcanoes, have been presented by Garcés *et al.* (2008), Matoza *et al.* (2009), Fee *et al.* (2010) and Matoza & Fee (2014). Near-field observations of the 2006 July 14–15 eruption and a discussion of the seismic and acoustic energy that it released are presented in this paper.

The following section describes both the seismic-acoustic network installed on Tungurahua volcano and its eruption on 2006 July 14–15. Section 3 presents the relationship between the seismic and acoustic intensities with their sources and determines the conditions needed to satisfy a linear relationship between them (Section 3.1), constructs the seismic and acoustic indices for monitoring purpose (Section 3.2), and develops a procedure to identify disturbances during an eruption, such as explosions or pyroclastic flows (Section 3.3). Details about processing steps and the corresponding results, as applied to our study case, are presented in Sections 4 and 5. Finally, in Section 6 two possible causes of a linear relationship between the acoustic and seismic intensities, that is, the existence of a common volcanic source and the acoustic wave coupling, are discussed.

2 TUNGURAHUA

2.1 Network and data

In July 2006 the seismic-acoustic network (Fig. 1a) on Tungurahua volcano (long: 78.45W, lat: 1.47S, 5023 m a.s.l.) was comprised of three stations, each one having an ACO TYPE 7144/4144 (0.01–10 s) acoustic sensor and a Guralp CMG-40T broad-band seismic sensor (0.02–60 s). The acoustic sensor was fixed 1.5 m above ground level, while the seismic sensor was buried at a depth of 1–2 m. The data from both sensors were digitized at 50 Hz. The sensor-digitizer systems provided a 0.02–20 Hz seismic and a 0.1–20 Hz acoustic flat-response.

The network was installed a few days (BRUN and BMAS1) or hours (BCUS) before the 2006 July 14–15 eruption, which is

the focus of this work. The installation of BCUS station was just being finished when the eruption started. The BCUS seismic sensor captured a strong signal at 22:31:30 GMT on July 14 caused by a team of technicians as they left the station, hereinafter called *cultural activity*. About 1.5 min later a strong explosion and the subsequent tremor marked the eruption onset (IGEPN 2006a).

2.2 The 2006 July 14–15 eruption

Several hundreds of explosions per day occurred before the paroxysmal phase. At 22:00 GMT of July 14 a researcher from the Geophysical Institute (IGEPN), working at Cusua town which is close to BCUS station, reported large magnitude ground displacements and that their 'vehicle was moving like a hammock' (IGEPN 2006a).

The sustained ejection phase started after an explosion at 22:33:00 GMT, leading to tremor with progressively increasing energy that lasted for roughly 4.3 hr. From satellite information a maximum 14.50–14.75 km a.s.l. height was estimated for the eruption column (Steffke *et al.* 2010), which is equivalent to 9.5–9.7 km above the summit. The volcanic jet was accompanied by a lava fountain (Fig. 1c) that accumulated around the summit, causing several pyroclastic flows (IGEPN 2006b), mainly on the W–NW flank (Fig. 1a). Based on ash deposit measurements, an emitted volume between 1.3×10^6 and 2.0×10^6 m^3 was estimated by Troncoso *et al.* (2006), which corresponds to a volcanic explosivity index VEI 2 (Newhall & Self 1982; Bustillos & Samaniego 2011).

Fig. 2 shows the waveforms of infrasound and seismic vertical components of the eruption. The marked pyroclastic flows (PF) and
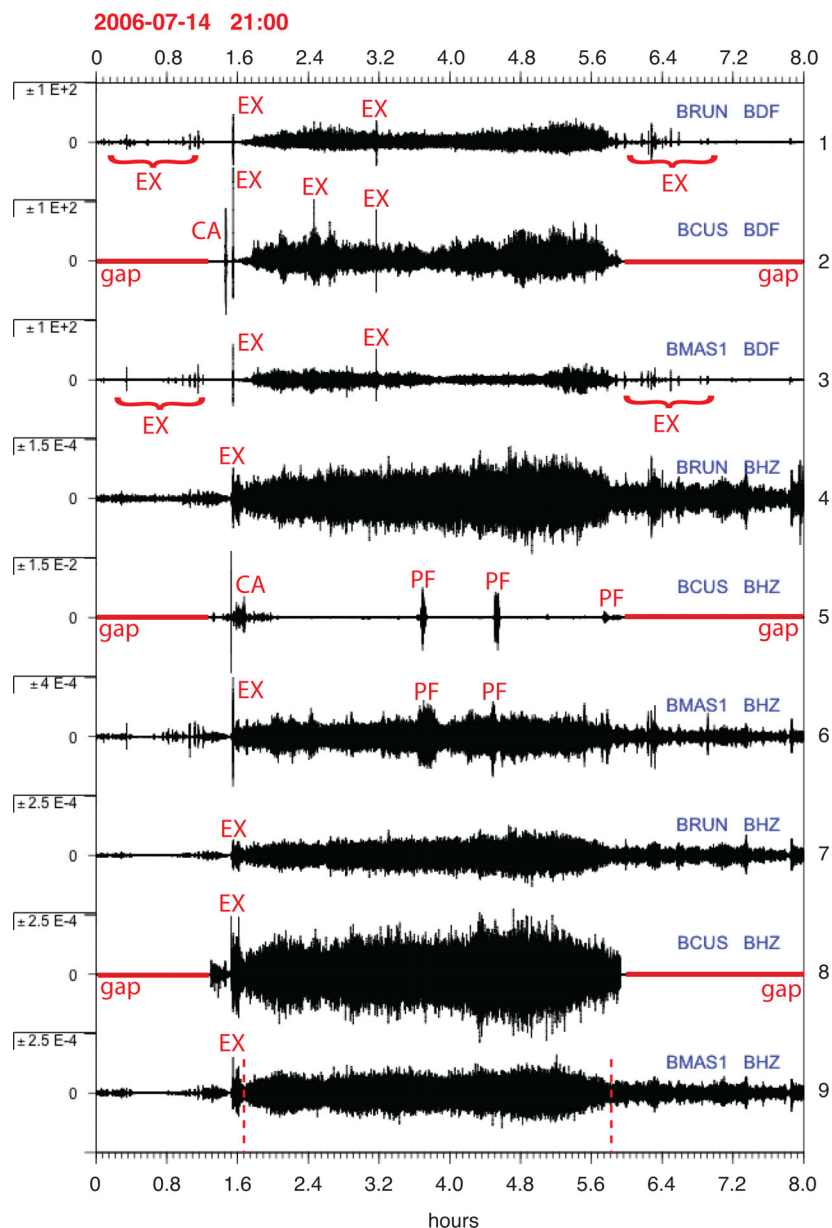

Figure 2. Waveforms of the eruption on 2006 July 14–15. Traces 1–3 (right vertical axis) are infrasound components (BDF, Pa) at all stations. Traces 4–6 are seismic vertical components (BHZ, m s^{-1}) without filtering and traces 7–9 are obtained after applying a low pass filter at 4 Hz. Symbols ± in the left vertical axis represent maximum and minimum amplitude values of each trace, centred at zero, either in Pa or m s^{-1}. Several events are marked as explosion (EX), pyroclastic flow (PF) or cultural activity (CA). Red dashed lines in trace 9 are the limits that define the eruption period. Records of BCUS station have gaps before and after the eruption.
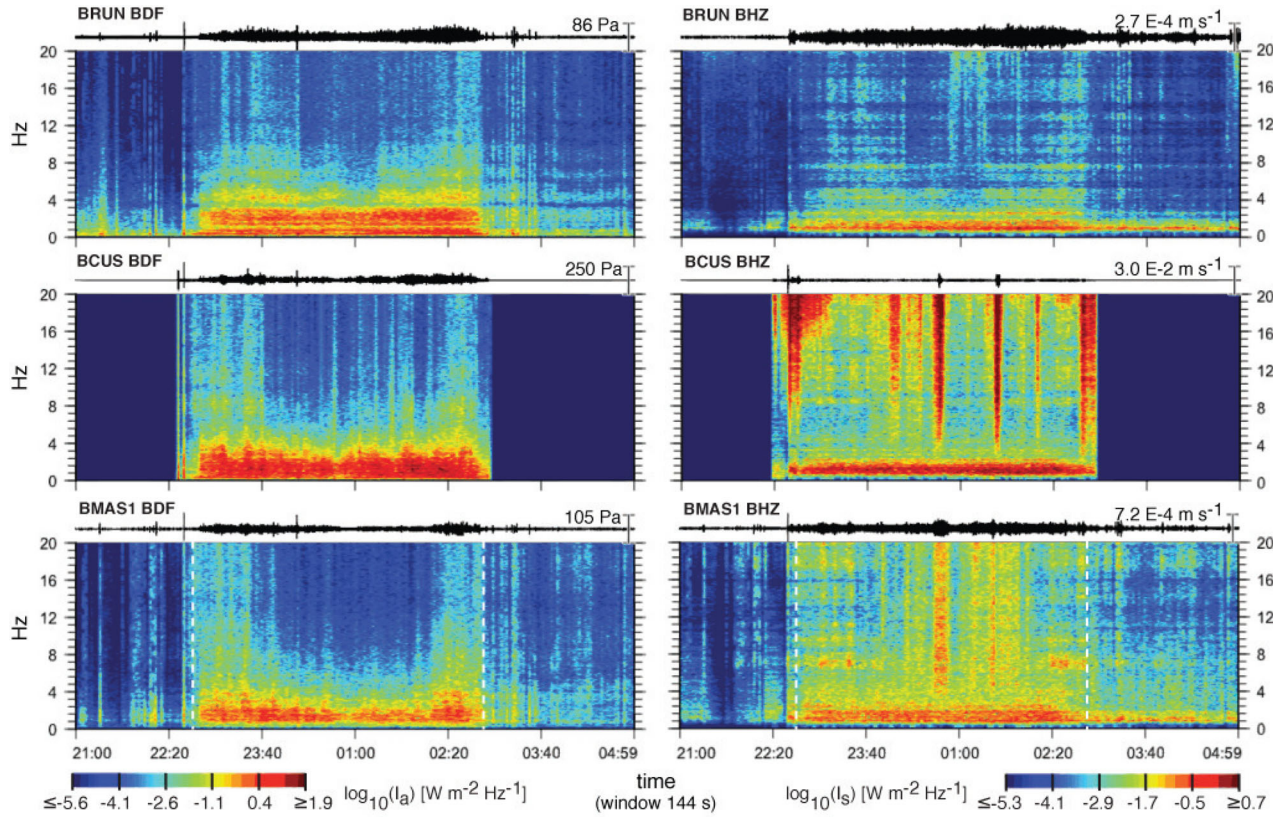
Figure 3. Intensity spectrograms of infrasound (left) and vertical seismic components (right). White dashed lines define the eruption period.

cultural activity (CA) were confirmed by field observers (IGEPN 2006a). Fig. 3 shows spectrograms of traces 1–6 of Fig. 2. The time interval between 22:40 on July 14 and 02:50 on July 15 contains almost the whole sustained ejection, which hereinafter is called *the eruption period*. Its limits appear as red vertical dashed lines in trace 9 of Fig. 2 and white vertical dashed lines in Fig. 3. Power spectra, normalized with their area, of the records during the eruption period are presented in Fig. 4.

3 ENERGY PARTITION

Our main focus in this work is to quantify the partitioning of energy into acoustic and seismic fractions during the sustained explosive eruption described in the previous section. In the following, after briefly reviewing empirical expressions for the acoustic power radiated by a jet, we define a similar relationship for the energy seismically radiated by the volcanic conduit, compute the ratio of the acoustic to seismic intensities, and define seismic and acoustic indices that clarify the nature of the energy scaling.

3.1 Acoustic and seismic radiation

To analyse the acoustic-seismic energy partitioning during a paroxysm we envisage the simplified volcanic system as depicted in Fig. 5. This sketch shows the key volcanic phenomena, specifically, conduit flow, fragmentation and the development of an eruption column. The turbulent multiphase flow regime, a result of fragmentation within the conduit, and the volcanic jet at the base of the eruptive column are both processes which radiate seismic and acoustic waves that are eventually recorded at the monitoring stations.

In early work Woulff & McGetchin (1976), using dimensional analysis, derived the following scaling relationships between radiated acoustic power and jet velocity of volcanic eruptions for three different type of sources:

$$\text{monopolar} \quad P_M = K_M \rho_a c_a^3 A \left(\frac{V}{c_a}\right)^4, \tag{1}$$

$$\text{dipolar} \quad P_D = K_D \rho_a c_a^3 A \left(\frac{V}{c_a}\right)^6, \tag{2}$$

$$\text{quadrupolar} \quad P_Q = K_Q \rho_a c_a^3 A \left(\frac{V}{c_a}\right)^8, \tag{3}$$

where A is the vent area, ρ_a the air density, c_a the air sound velocity, V the jet velocity and K_M, K_D, K_Q are empirical constants. These quantities (eqs 1–3) are proportional to square, cubic and fourth powers of the dimensionless kinetic measure $E_k = (V/c_a)^2$, the square of the Mach number. Pulsations of a small body in a fluid, or a sudden explosion, where the rate of increase of fluid per unit of volume is time dependent, are sources represented by monopoles (Howe 2003). Other acoustic sources like vibrating bars, or displacement of solids in a fluid, usually are represented by dipoles. In these cases the fluid is forced producing pressure changes at the fluid–solid boundary, which then are radiated as acoustic waves. Finally, quadrupoles arise in fluid-fluid interactions, like in entrainments, where although the action–reaction force sum between fluids is neglected, local instabilities are produced, which form the source of the acoustic radiation.

More recent experiments on heated jets, however, show that the quadrupolar power radiation may scale with jet velocity V with exponents different than 8, possibly due to a dependence on the ratio
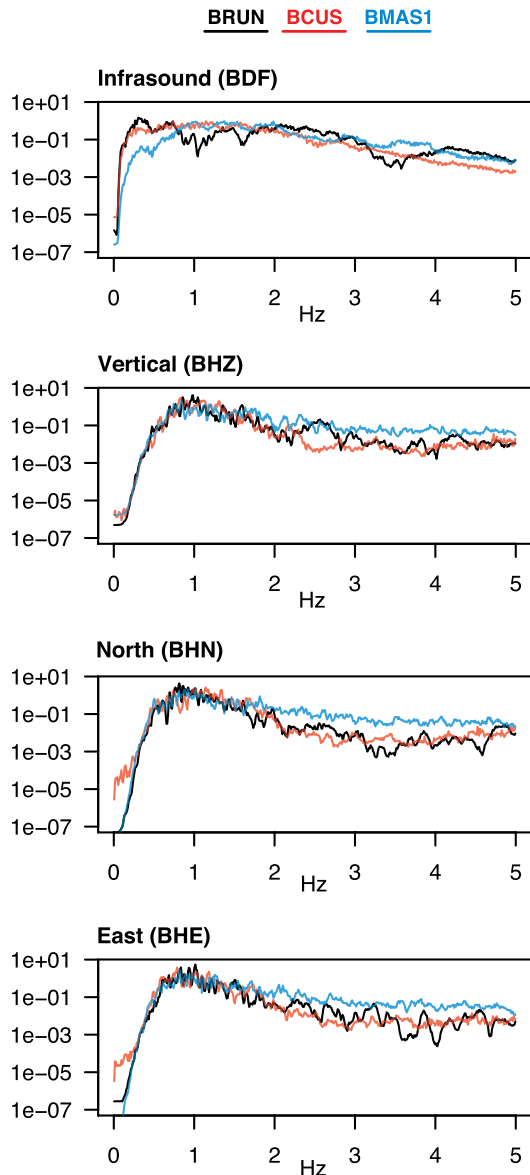
BRUN BCUS BMAS1

Figure 4. Normalized power spectra of infrasound and seismic components (vertical, north and east) for the eruption period (Jul 14, 22:40–Jul 15, 02:50).

Figure 5. Sketch illustrating acoustic and seismic phenomena during a sustained phase of an explosive eruption, a paroxysm. Seismic waves are caused by the interaction of the magmatic mixture with the conduit walls, whereas in the near-field region the acoustic waves are thought to come from fine-scale turbulences or solid–fluid interactions, at an angle $\theta > 90°$ (e.g. Tam *et al.* 2008). LST: large scale turbulence. The symbols $\oplus$ and $\ominus$ at bottom and top of the fragmentation region, respectively, represent pressure changes.

between the jet and the reservoir temperatures, T_j/T_r, and on the detection angle θ (Viswanathan & Czech 2009). The importance of these observations on volcanic jets has been highlighted by Matoza *et al.* (2013) who show that the estimation of total power may be subjected to large errors if both directivity and temperature parameters are not taken into account. Following their suggestion, we write the time-dependent acoustic intensity $I_a(t)$ for a given station as

$$I_a(t) = \alpha_a E_k^{n_a}(t), \qquad (4)$$

where $E_k(t) = (V(t)/c_a)^2$ is time dependent, α_a is a parameter depending on source-station distance, θ and T_j/T_r. The exponent n_a is also a parameter depending on θ and T_j/T_r.

The radiated seismic energy, on the other hand, is affected by the interaction between the multiphase eruptive mixture and the conduit walls. Assuming that the eruptive mixture can be described as a homogeneous gas, such interaction could be characterized by the scaling in eq. (2). Thus, the acoustic waves within the conduit may
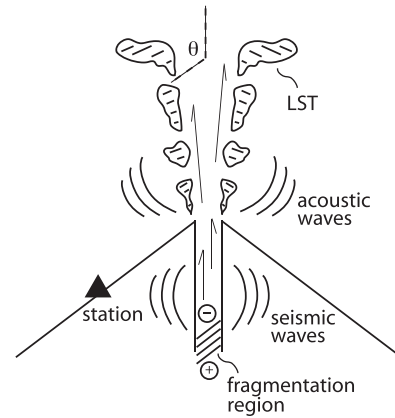
be reflected, back and forth, transversally to the conduit axis, transmitting an amount of energy that depends on the impedance contrast between the fluid and the volcanic edifice. Because the station is in the near field, the conduit may be considered as a distributed source, which can cause an angular dependence in the recorded seismic intensities. Then, taking into account that the seismic intensity would be dependent on mixture velocity, we define

$$I_s(t) = \alpha_s E_k^{n_s}(t), \qquad (5)$$

where the parameters α_s and n_s, dependent on source-station distance, directivity, mixture–reservoir temperature ratio and impedance contrast, are assumed to be time independent.

We now pose the hypothesis that acoustic and seismic energies, and consequently the intensities measured at each station, scale proportionally. That is, their ratio will be time independent. Thus, from eqs (4) and (5) we define the volcano acoustic–seismic ratio (VASR) of intensities as

$$\eta(t) = \frac{I_a(t)}{I_s(t)} = \frac{\alpha_a}{\alpha_s} E_k^{n_a - n_s}(t), \qquad (6)$$

which is analogous to the definition based on source energies (e.g. Johnson & Aster 2005). It follows then that their corresponding intensities should be related by the same constant η_0, leading to $I_a(t) = \eta_0 I_s(t)$. Such a relation is true only if $\eta_0 = \alpha_a/\alpha_s$ and $n_a = n_s$, which implies that the source type (monopole, dipole, quadrupole) for the radiated seismic and acoustic energy is the same.

3.2 Acoustic and seismic indices

In this section we construct the acoustic and seismic indices, $\pi_a(t)$ and $\pi_s(t)$ respectively, and determine their relationship with the corresponding source type: monopolar, dipolar or quadrupolar. An index is a dimensionless measure, relative to a fix reference value used as unit, to compare different stages of a process (e.g. Kendall 1969). We use as references the acoustic and seismic average intensities during a period T, which is the eruption duration of the

paroxysm, namely,

$$\bar{I}_a = \frac{1}{T} \int_0^T I_a(t)\,dt = \frac{\alpha_a}{T} \int_0^T E_k^{n_a}(t)\,dt, \qquad (7)$$

$$\bar{I}_s = \frac{1}{T} \int_0^T I_s(t)\,dt = \frac{\alpha_s}{T} \int_0^T E_k^{n_s}(t)\,dt, \qquad (8)$$

where eqs (4) and (5) have been used. Then, we define the acoustic and seismic indices as

$$\pi_a(t) = \frac{I_a(t)}{\bar{I}_a} \quad \text{and} \quad \pi_s(t) = \frac{I_s(t)}{\bar{I}_s}. \qquad (9)$$

If the source types are the same ($n_a = n_s$), the acoustic and seismic energies scale proportionally and any linear combination of instant intensities, in particular their average intensities $\bar{I}_a$ and $\bar{I}_s$, follows the same proportion. This is because the integrals in eqs (7) and (8) are the same and cancel out in such proportions. Thus

$$\frac{\bar{I}_a}{\bar{I}_s} = \frac{\alpha_a}{\alpha_s} = \eta_0, \qquad (10)$$

which comparing with eq. (6) we conclude necessarily that

$$\pi_a(t) = \pi_s(t). \qquad (11)$$

Conversely, if we assume that the indices are equal at each time t, then from their definition (9) we have that the VASR is constant,

$$\frac{I_a(t)}{I_s(t)} = \frac{\bar{I}_a}{\bar{I}_s}. \qquad (12)$$

Using the intensity definitions (4) and (5) and $E_k(t) = (V(t)/c_a)^2$, eq. (12) gives the ejection velocity as function of time t,

$$V(t)^{2(n_a - n_s)} = \frac{\bar{I}_a}{\bar{I}_s} \frac{\alpha_s}{\alpha_a} c_a^{2(n_a - n_s)}. \qquad (13)$$

As the right-hand-side of this equation is time independent, the ejection velocity must be either constant or the acoustic and seismic source types must be the same ($n_a = n_s$). Real cases, such as the one studied here, involve time variable intensities and velocities. Therefore from equal seismic and acoustic indices, we conclude that the acoustic and seismic sources share the same type.

In this section we have demonstrated that the equality of indices is a necessary and sufficient condition to infer that the acoustic and seismic source types are identical. However, we have not yet considered the possibility that the records are collected at the stations on the air–ground boundary, which involves coupling effects (Ichihara *et al.* 2012). This case is analysed later in Section 6.2 in terms of the expected intensities.

3.3 Disturbances in sustained eruptions (outliers)

It is important to realize that during the course of a sustained explosive phase, strong explosions and seismic events should be expected. In such cases, large variations in VASR values are likely to occur. These extremely high or low ratios would appear as outliers in the VASR time-series and a linear scaling between acoustic and seismic intensities can hardly be expected. Hence, their identification is needed before applying the equations of Section 3.2.

The outlier identification procedure starts by forming a time-series using short-length time windows (see Section 4) from eq. (6). Let η_t be this time series which, due to its definition, is formed by positive values. We use the sample median, $M(\eta_t) = M_\eta$, and the sample median absolute deviation, $D(\eta_t) = D_\eta = 1.4826\,M(|\eta_t -$

$M_\eta|)$ (Leys *et al.* 2013), to define the upper limit $M_\eta + 3D_\eta$ over which a value is considered an outlier. The lower limit is computed as the inverse of the upper limit of the time series formed by the inverse values η_t^{-1}. We define outliers as those values that do not belong to the interval

$$\frac{1}{M_{\eta^{-1}} + 3D_{\eta^{-1}}} \le \eta_t \le M_\eta + 3D_\eta. \qquad (14)$$

Although this equation can detect strong events, small ones might be embedded within the time series, for instance small explosions. Because such signals are time-localized transients they are rich in high frequencies compared to the more slowly varying jet generated VASR. In such a case, the application of a high pass filter is useful. Thus, by applying a zero-shift high pass filter to η_t a new time-series $\tilde{\eta}_t$ is obtained, and we define these additional outliers as those that belong to the interval

$$|\tilde{\eta}_t| > 3D_{\tilde{\eta}}. \qquad (15)$$

The appendix provides an example of a synthetic time series, where intrusive values to be detected were added. Only some of these are detected by eq. (14), however after applying eq. (15) all of them are identified.

4 PROCESSING STEPS, CORRECTIONS AND ASSUMPTIONS

Before computing the VASR time-series and considering physical interpretations, some important corrections and assumptions need to be made explicit. What follows are the steps for evaluating the VASR.

(i) *Site effects*. The influence of site effects on the seismic signals needs to be corrected for two reasons. First, to reduce the effect of local geological heterogeneity on seismic signals to ensure that comparisons between stations become meaningful, and second, to reduce acoustic-seismic coupling, mainly because the backscattering also tends to reproduce site effects. However, some remnant coupling effects still might exist in the seismic records. Palacios *et al.* (2015) discussed in details these effects for the eruption here studied, demonstrating that coupling effects are most significant at frequencies higher than 4–5 Hz. Due to restrictions at low frequency of the site correction method (Palacios *et al.* 2015), caused by the presence of micro-seismic noise, we will analyse the signal filtered in the range 0.4–4 Hz. This range includes almost all seismic energy before and after site corrections (Fig. 4).

(ii) *Time shift correction*. To compute $I_a(t)$ and $I_s(t)$ at a common time t, a correction related to the source-station wave traveltime is needed. Let us represent the average acoustic and seismic effects of distributed sources with two centroids or point sources, one located at the summit and the other within the conduit, respectively. These two sources are causally related, assuming that the fragmentation process is ultimately the origin of their corresponding signals (Fig. 5). If δt_S is the traveltime from the seismic source to the station, δt_A from the acoustic source to the station, and δt_C from the seismic to the acoustic source, along the conduit, then the seismic and acoustic records at time t, originated at $t - \delta t_S$ and $t - \delta t_A - \delta t_C$, respectively. Their difference, $\Delta = (t - \delta t_S) - (t - \delta t_A - \delta t_C) = \delta t_A + \delta t_C - \delta t_S$, is the delay of the acoustic signal compared with the seismic signal. The correction shifts the acoustic record earlier in time by Δ. This quantity is constrained by estimating the pressure wave velocity along the conduit, equal to $V + c_a$, due to the advection caused by the ejecting flow on the pressure waves originated in

the fragmentation region. Matoza *et al.* (2013) show that inferring V from a single station leads to values with large uncertainties. They also used the 2006 July 14–15 eruption of Tungurahua as a study case, obtaining V values ranging from few tens m s^{-1} to 450 m s^{-1}. For our correction we use average ejection velocities V between 100 and 300 m s^{-1}, a seismic source between 1 and 3 km beneath the summit and an acoustic source at the summit. Then, using the corresponding station locations, the difference $\delta t_C - \delta t_S$ has values between 1.0 and 4.5 s. Therefore, the correction with $\Delta \sim \delta t_A + 3$ s may have an error of roughly two seconds that, compared with the window length $w = 60$ s, does not modify significantly the intensities computed.

(iii) *Seismic and acoustic intensity time series*. Each time-series is constructed choosing 60 s length windows, 50 per cent overlapped, assuming that the eruption energy does not change significantly within the window period. Shorter windows are not selected because some events, like explosions or earthquakes, usually last several tens of seconds. The acoustic and seismic intensity time-series, $I_a(t)$ and $I_s(t)$ (in W m^{-2}), respectively, are computed as the average intensity of sample records within each window, namely,

$$I_a(t) = \frac{1}{w\rho_a c_a} \sum_{\tau=t-w/2}^{t+w/2} p^2(\tau)\,\delta\tau, \tag{16}$$

$$I_s(t) = \frac{\rho_s c_s}{w} \sum_{\tau=t-w/2}^{t+w/2} v^2(\tau)\,\delta\tau, \tag{17}$$

where $\rho_a = 1.25$ kg m^{-3} and $\rho_s = 2500$ kg m^{-3} are densities of air and rock, $c_a = 337$ m s^{-1} and $c_s = 2000$ m s^{-1} are the air wave velocity and shear wave velocity in the volcanic edifice, respectively, w is the window length, $\delta\tau$ the time interval between consecutive samples, t the central window time, p the acoustic pressure in Pa, and v the magnitude of the recorded ground velocity (determined by all components) in m s^{-1}. Note that if N is the number of samples per window, then $w/\delta t = N - 1$. After replacing continuous by discrete values, eqs (4), (5), (6), (9) and (11) are now considered as times series.

(iv) *Computing VASR and indices*. The time-series of VASR is computed by eq. (6). The outliers are determined and excluded when the seismic and acoustic mean intensities are calculated and using only information of the eruption period. Finally, the indices given by eq. (9) are constructed.

5 RESULTS

5.1 Volcano acoustic–seismic ratio

The VASRs computed at all stations are shown in Fig. 6. The average intensities needed in eq. (10) to compute η_0 include only those windows where the seismic and acoustic intensities tend to be related proportionally; explosions, pyroclastic flows or strong seismic events are excluded as is described in Section 3.3. Seismic records are filtered either in the range 0.4–20 Hz for detecting explosions (coupled in the soil) and near pyroclastic flows, or in the range 0.4–4 Hz for detecting strong seismic events. The time-series η_t presented in Fig. 6 uses the range 0.4–4 Hz for seismic intensities and 0.1–20 Hz the acoustic ones. For our case, the time-series $\tilde{\eta}_t$ is obtained from η_t applying a zero-shift high-pass Butterworth filter at the corner defined by 0.1 cycles per sampling time interval (cps). To compute the seismic intensities all components are summed at each station.

The grey regions (Fig. 6) calculated for BRUN ($0.9 \leq \eta_t \leq 5.3$), BCUS ($0.3 \leq \eta_t \leq 2.1$) and BMAS1 ($0.2 \leq \eta_t \leq 2.0$) give an idea of the VASR variation. Interestingly, such VASR variation is significantly smaller during the sustained phase than periods before or after the it, when several explosions are included (traces 1–3 of Fig. 2).

5.2 Indices

Seismic and acoustic indices (eq. 9) are shown in Fig. 7. The mean intensities needed for their computation at BRUN ($\bar{I}_a = 0.044$; $\bar{I}_s = 0.019$ W m^{-2}), BCUS ($\bar{I}_a = 0.144$; $\bar{I}_s = 0.162$ W m^{-2}) and BMAS1 ($\bar{I}_a = 0.023$; $\bar{I}_s = 0.040$ W m^{-2}) are represented by the levels $\pi_a = 1$ and $\pi_s = 1$, denoted by horizontal dashed lines. These values are determined with the non-outliers windows within the eruption period.

Fig. 8 presents smoothed seismic and acoustic indices for all stations. The smoothing was performed averaging the indices with a 5 min moving window. This average uses the values of the standard Normal probability function, across $-2, -1.5, \ldots, 1.5, 2$, as weights, which are scaled to sum up to one. This figure shows more similarity between the seismic records than the acoustic ones, which is useful to understand the relationship between seismic and acoustic signals to be discussed in the next section.

6 DISCUSSION

During a sustained eruption, both seismic and acoustic records can be strongly influenced by processes occurring local to the station. After correcting site effects, the seismicity caused by cultural activity and pyroclastic flows that strike the ground while descending close to a station, is clearly identified due to its high frequency content (traces 5 and 6 in Fig. 2). On the other hand, the residual low-frequency information (below 4 Hz, traces 7–9 in Fig. 2) shows a strong similarity between stations (Fig. 8), suggesting that it originated from common internal volcanic seismic sources. We are interested here in discussing what relationship the seismic energy might have with the acoustic energy, in particular whether such a relationship is linear, as described by eq. (11).

6.1 Correlation between seismic and acoustic intensities

The VASR in Fig. 6 shows less variations during the eruption period than before or after it, which supports the hypothesis that there exists a linear correlation between the acoustic and seismic intensities. Hereinafter correlations are evaluated using the Pearson product-moment coefficient, which is the normalized covariance of the variables (e.g. Shumway & Stoffer 2010). For those intensities belonging to the eruption period, with outliers removed, their correlation is significant for BRUN (0.60) and BCUS1 (0.56). However, it is too low for BMAS1 (0.05). Fig. 7 shows that the behaviour in time of acoustic and seismic indices are roughly similar in BRUN and BCUS, unlike that shown for BMAS1. The discrepancy is clearly seen in the top panel of Fig. 8. The maximum acoustic intensities at BCUS (at 01:49) and BMAS1 (at 02:17) are sufficiently separated in time, suggesting that additional phenomena could be causing the lack of coincidence between the acoustic indices. A number of phenomena, including changes in acoustic source position, changes in meteorology or topographic characteristics may act to cause intrastation differences in intensity. Further studies are required in order
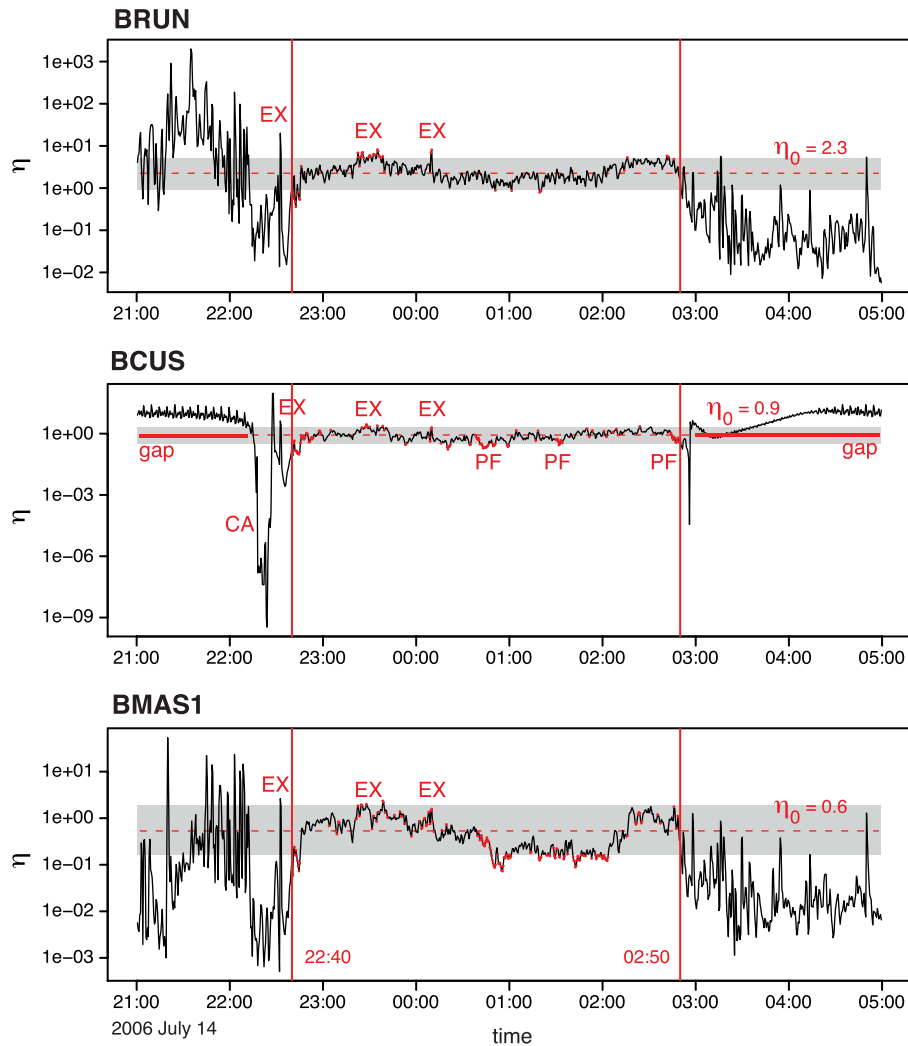
Figure 6. Volcanic acoustic seismic ratios η_t. Several explosions (EX), pyroclastic flows (PF) and cultural activity (CA) are marked. Red vertical lines state the initial and final time of the sustained eruption and those outliers within this period appear as red dots. Grey regions represent η_t variation as described by eq. (14). Horizontal red dashed lines are the ratio of mean intensities.

to gain a better understanding of how such phenomena influence the spectral difference of the acoustic records (Figs 3 and 4).

6.2 Influence of coupling on acoustic and seismic records

6.2.1 Expected intensities analysis

A linear correlation between the seismic and acoustic intensities could in principle be expected due to the coupling either between acoustic waves and the ground or seismic waves and the air (Ichihara *et al.* 2012). In this section we analyse both cases in terms of expected intensities that are transmitted in the air–ground boundary and compare them with the existence of a common cause.

The first case, the arrival of acoustic waves at the ground, is an impact-like process, which is generally better observed in the high-frequency components of seismic records. However, whether a low frequency response is elicited or not depends on the site frequency response function around each station, which has been corrected in this study. The following three arguments support the hypothesis that the recorded seismicity below 4 Hz (Fig. 8) is primarily caused

by internal volcanic sources. (a) Assuming the coupled acoustic waves are dominant in the seismic records, the inter-station differences observed between the acoustic indices should be translated into similar differences between the seismic indices (Fig. 8), which is not the case. (b) The seismicity was strong enough to be detected by stations on other distant volcanoes. For example, the monitoring network of Cotopaxi volcano, located 86 km north of Tungurahua, includes four stations (BTAM, BVC2, BREF and BNAS) with seismic and infrasound sensors with identical characteristics to those used in this study (Kumagai *et al.* 2007). Fig. 9 compares the average of seismic indices from the four Cotopaxi stations, with the average of seismic indices from the three Tungurahua stations. Their strong correlation suggests a common source and reaches a maximum value (0.88) for a lag of the Cotopaxi time-series between 30 and 90 s, which can be explained by the propagation of surface seismic waves between the volcanoes. If coupled acoustic waves had been the origin of Cotopaxi records, a 4.3 min lag should be expected because we know the distance between the volcanoes and the acoustic wave velocity, which has not been observed. Furthermore, the acoustic records of Cotopaxi stations do not show any relevant change during the eruption period. (c) The coupling would not be energetic enough to explain the seismic signals. In order to have an
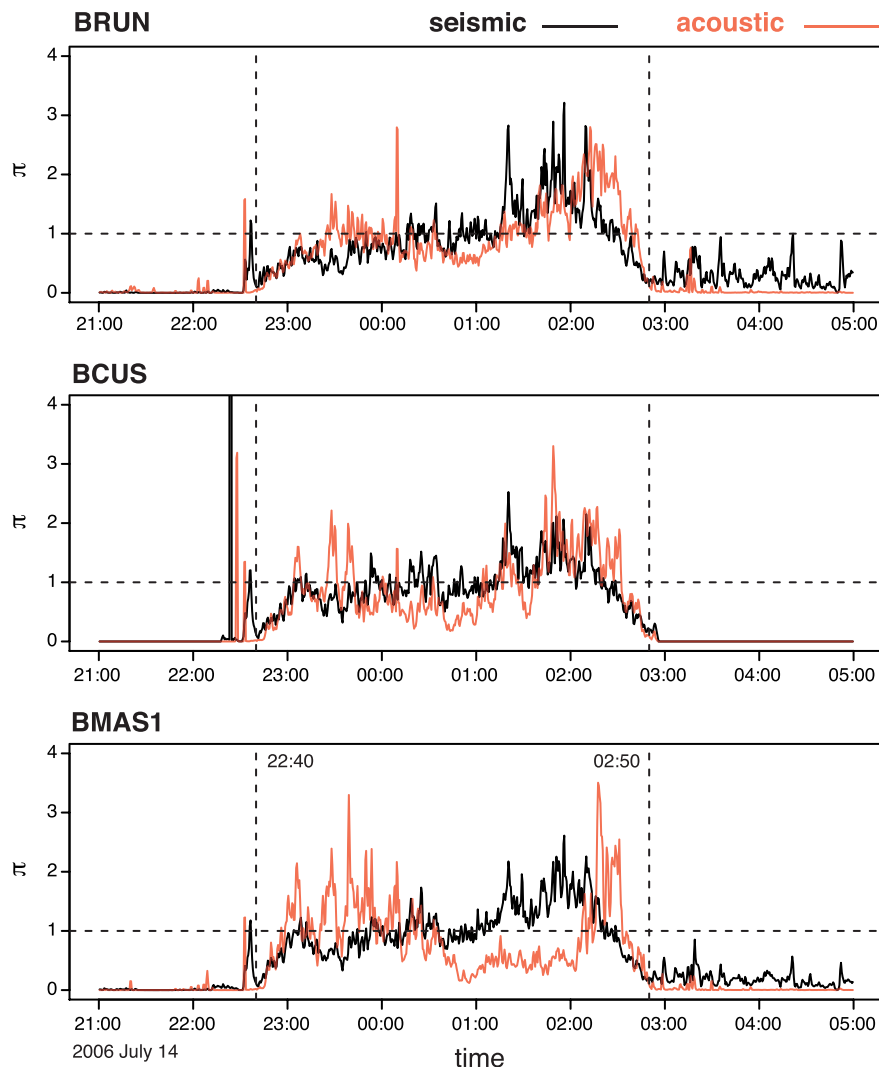
Figure 7. Seismic and acoustic indices at each station. Vertical dashed lines define the period when the sustained eruption was observed. Each horizontal dashed line represents the reference level, or mean intensity.

approximation of the transmitted intensity during the coupling and its comparison with the recorded seismic intensity, let us consider an acoustic wave striking the ground at vertical incidence, which is the case of maximum transmission. If $\mathcal{R}$ and $\mathcal{T}$ are the reflexion and transmission coefficients for the wave amplitudes, then their corresponding intensity coefficients $\mathcal{R}^2$ and $\mathcal{T}^2$ are related by the expression (e.g. Stein & Wysession 2003)

$$\mathcal{T}^2 = 1 - \mathcal{R}^2 = 1 - \left(\frac{\rho_a c_a - \rho_s c_s}{\rho_a c_a + \rho_s c_s} \right)^2, \qquad (18)$$

where the product of $\rho_a = 1.25$ kg m^{-3} and $c_a = 337$ m s^{-1} defines the acoustic impedance. If we consider two limiting cases for the soil impedance, one describing fully dense rock with density $\rho_s = 2500$ kg m^{-3} and wave velocity $c_s = 2000$ m s^{-1}, and other representing highly porous sediments with $\rho_s = 1500$ kg m^{-3} and $c_s = 400$ m s^{-1}, then

$$3.37 \times 10^{-4} < \mathcal{T}^2 < 2.80 \times 10^{-3}. \qquad (19)$$

In addition to the vertical incidence, the maximum transmission for the mean acoustic intensities given in Section 5.2 is obtained

with the upper limit of $\mathcal{T}^2$, this is for porous sediments. The mean seismic intensities needed for the comparison computed with the lowest impedance are $\bar{I}_s = 0.0023$ W m^{-2} (BRUN), $\bar{I}_s = 0.0194$ W m^{-2} (BCUS) and $\bar{I}_s = 0.0048$ W m^{-2} (BMAS1). We found that the maximum proportions of transmitted intensity compared with the recorded seismic intensity are 5.4 per cent (BRUN), 2.1 per cent (BCUS) and 1.3 per cent (BMAS1).

The second coupling case occurs when seismic waves arrive at the air-ground boundary, interacting with the atmosphere and transmitting air pressure waves. In our data the seismic intensities are similar or smaller than the acoustic intensities. This combined with the small transmission coefficients given by eq. (19), produces transmitted intensities at least three orders smaller than the recorded acoustic intensities. Consequently, we can neglect the contribution of coupled seismic waves in the acoustic records.

In this section, using either the maximum expected seismic or acoustic intensity that is transmitted at the air-ground boundary, we have demonstrated that the low frequency (0.4–4 Hz) seismic waves and the acoustic waves recorded at all stations cannot be explained by coupling processes. Therefore, the observed correlations are dominated by non-coupled waves, with a common
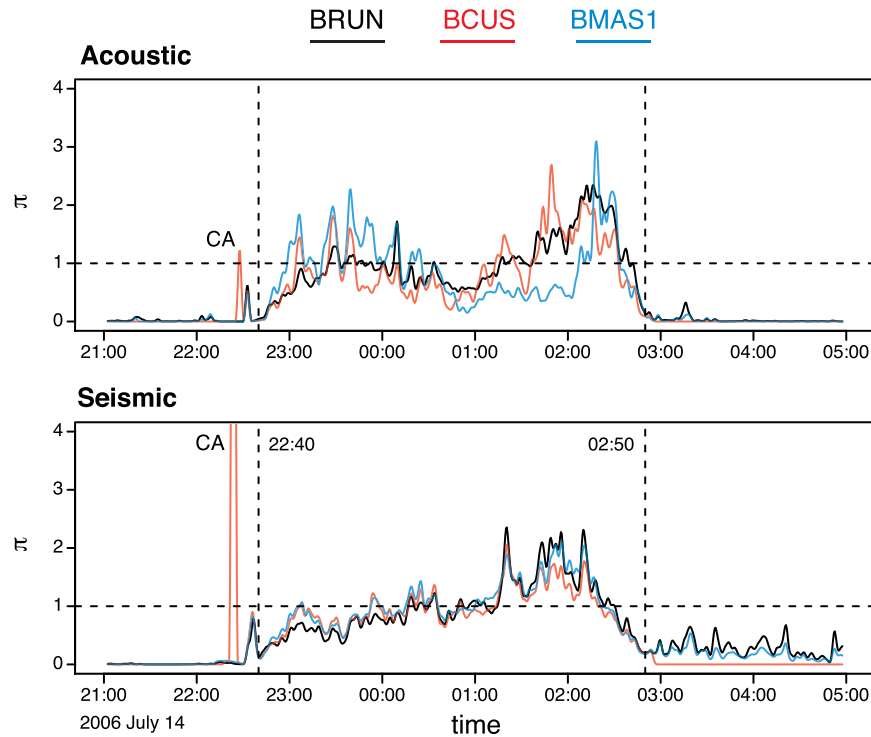
Figure 8. Smoothed acoustic and seismic indices compared between stations. CA: cultural activity at BCUS station.
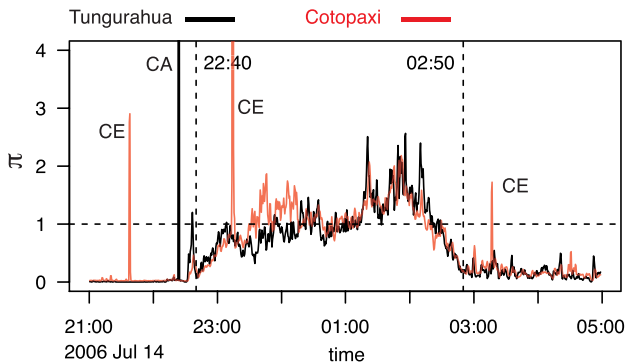

Figure 9. Average seismic indices Tungurahua and Cotopaxi stations. Three Cotopaxi local events (CE) and cultural activity (CA) at Tungurahua volcano are marked.

origin that we hypothesize is the sustained fragmentation during the eruption.

6.2.2 Spectral analysis

Exploring the frequency ranges where couplings occur also contributes to a better record interpretation. Ichihara *et al.* (2012) use the cross-correlation between the seismic and acoustic waves, from co-located sensors, to study coupling effects. This analysis is extended to the spectral domain by Matoza & Fee (2014), who use the coherence (its square amplitude and phase) to determine the frequency regions where couplings occur. These authors study the 2006 July 14–15 eruption with records collected by an infrasound array and a co-located seismic sensor installed 36.9 km south from Tungurahua volcano. They explore within the frequency range 0.3–5 Hz. They also notice two frequency bands of seismic tremor,

0.3–1.2 Hz and 1.6–2.5 Hz, whereas from our stations the energy is concentrated below 2 Hz, after site effect corrections (Figs 3 and 4). They also find square coherence amplitudes roughly between 0.4–0.6 during the strongest period of the eruption for frequencies over 2 Hz, however cross-correlations for 0.3–5 Hz waves are significant. Because of these results they conclude that the seismic waves are likely a complex mix between sub-surface waves coming from volcanic sources and air-ground coupled waves. A lag time analysis of recorded intensities between two seismic stations, one in near field and other in far field, similar to that shown in Fig. 9 where Cotopaxi and Tungurahua stations were used, also may be useful to figure out if the far field seismic records of Matoza & Fee (2014) are dominated or not by sub-surface waves.

Fig. 10 shows square amplitudes and phases of coherence between vertical seismic and infrasound components, during the paroxysm, from our near field stations. They were computed with non-overlapped 60 s windows for the range 0.4–4 Hz. Couplings appear at BRUN station over 2 Hz, which in part explains why the maximum expected intensity transmitted to the ground (Section 6.2.1) is larger at BRUN (5.4 per cent) station. Fig. 11 shows cross-correlograms constructed with 60 s moving windows. Values of vertical axes are lag times k of the vertical seismic component (BHZ) relative to the infrasound component (BDF). Cross-correlograms constructed with signals filtered in a wide range (for instance 0.4–4 Hz, see also fig. 17c in Palacios *et al.* 2015) could include couplings in a more restricted frequency band (for instance, 2–3.5 Hz at BRUN) showing low correlation values. After identifying the coupling frequency band, couplings are highlighted in the cross-correlogram constructed for that band. This is the case of BRUN station for 2–3.5 Hz, where even several explosions before and after the paroxysm have been clearly identified. Coupling frequency bands are not the same for all stations, which may depend on site properties (Palacios *et al.* 2015) and topographic conditions.
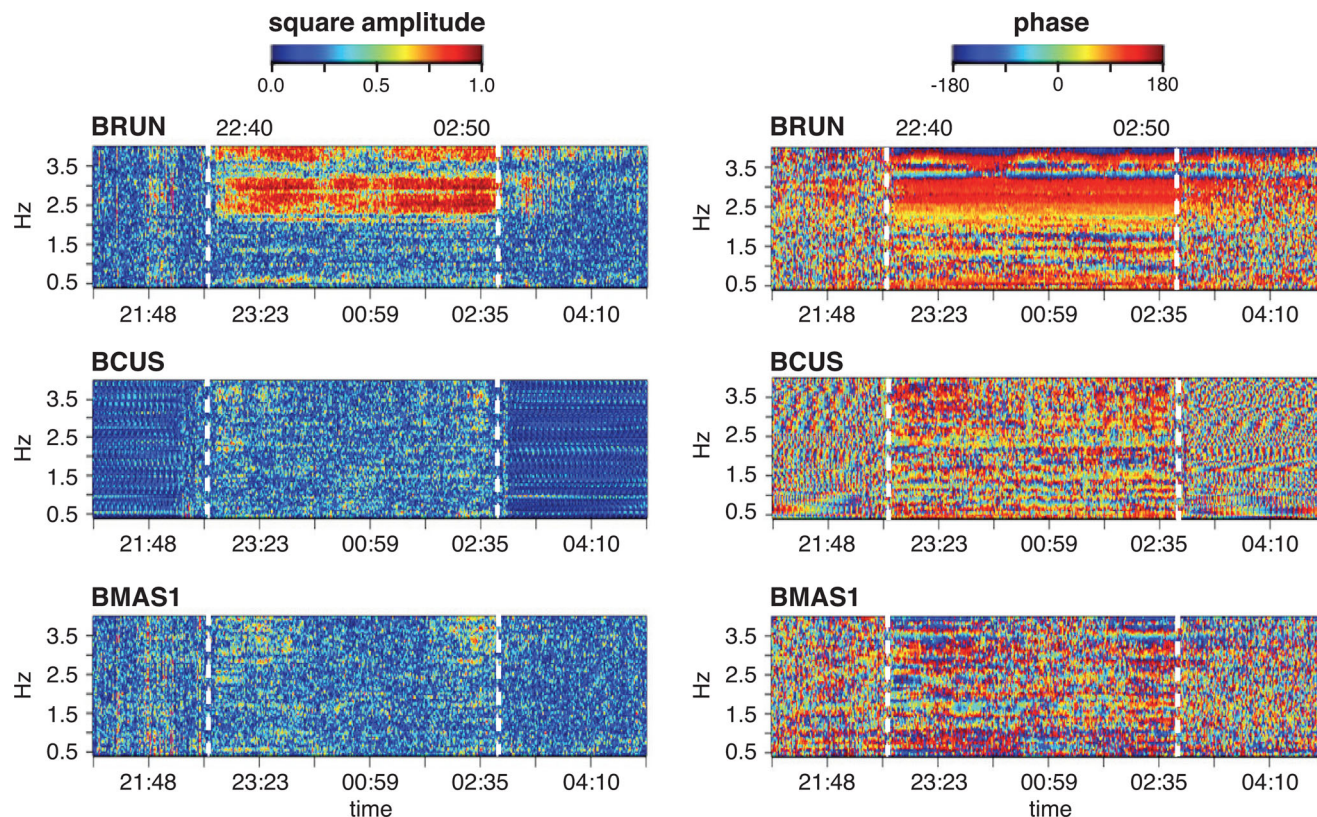
Figure 10. Square amplitudes and phases of coherence between the vertical seismic component (BHZ) and the infrasound component (BDF), at each station, of 2006 Jul 14 paroxysm. Non-overlapped 60 s windows were used. Vertical white dashed lines mark the initial (22:40) and final (02:50) eruption time.

Due to the lack of overlapping between the frequency band 0.4–2 Hz of the seismic tremor caused by internal volcanic sources, and coupling frequency band 2–3.5 Hz at BRUN station, we consider that below 2 Hz the signal is decoupled. However such decoupling is only an approximation, which is justified assuming that the arriving energy from internal sources is much larger than that transferred by air wave couplings. A more precise decoupling procedure computes the coupled signal and extracts it from the original records. In our case the presence of coupled components are minimized after correcting the site effects (see the frequency response functions of BRUN, fig. 5 in Palacios *et al.* 2015). A decoupling model still is required and may be considered in further studies.

6.3 Use of the seismic–acoustic correlation for monitoring volcanoes

We argue that two processes appear to contribute to the correlation between the seismic and acoustic records. First, an approximated linear partition of the source energy released by the fragmentation into seismic and acoustic components, and second, the coupling of the acoustic waves into the ground, both being dominant within different frequency ranges. For monitoring purposes, the concurrence of both processes may be helpful, particularly in the case of a lack of visibility, because a sustained correlation of acoustic and seismic records appears only if the magma is being ejected into the atmosphere, pointing to the possibility of pyroclastic flow generation. Indeed, in our case, during the first hours of the eruption the volcano was completely cloudy (IGEPN 2006b) hampering the hazard assessment.

Fig. 12 presents seismic and acoustic indices computed with filtered data in the frequency ranges discussed in Section 6.2.2. Top panels (0.4–4 Hz) show correlated seismic and acoustic indices considering both only the seismic vertical component or all seismic components. Second and third rows correspond to the decoupled seismic signal (0.4–2 Hz) and coupled seismic signal (2–3.5 Hz), respectively. Both cases show correlations. For the first case we hypothesize that it is explained by the occurrence of a common process, mainly the fragmentation within the volcanic conduit, which produces sub-surface seismic waves and acoustic waves. The second case is related to coupled air waves, according to the results discussed in Section 6.2.2. Note that the total coupled seismic intensity (right panel, 6.4×10^{-4} W m^{-2}), represent only 3.6 per cent of the decoupled seismic intensity (right panel, 1.8×10^{-2} W m^{-2}).

Correlations and coherences are useful measures to reveal similar behaviours between seismic and acoustic signals. However, due to their definitions use cross-covariance (e.g. Shumway & Stoffer 2010) normalized with the standard deviation of the involved variables, the information about signal amplitudes is lost. Because it is important for monitoring to have an idea as to the size of an ongoing eruption, the amplitude information must be preserved. Our index definition (see eq. 9) satisfies such conditions. Thus, in Fig. 12 we can observe simultaneously the intensity and correlation levels. Implementation of these indices require to know the seismic and acoustic reference levels, therefore, at least the information of one previously known paroxysm may be used for comparisons.

Bottom panels in Fig. 12 are computed using seismic signals without site effect corrections. Then, the correlation is explained by both the fragmentation process and amplified coupled records (mainly those belonging to the frequency range 2–3.5 Hz). Without site corrections, the amplification of coupled seismic records occurs
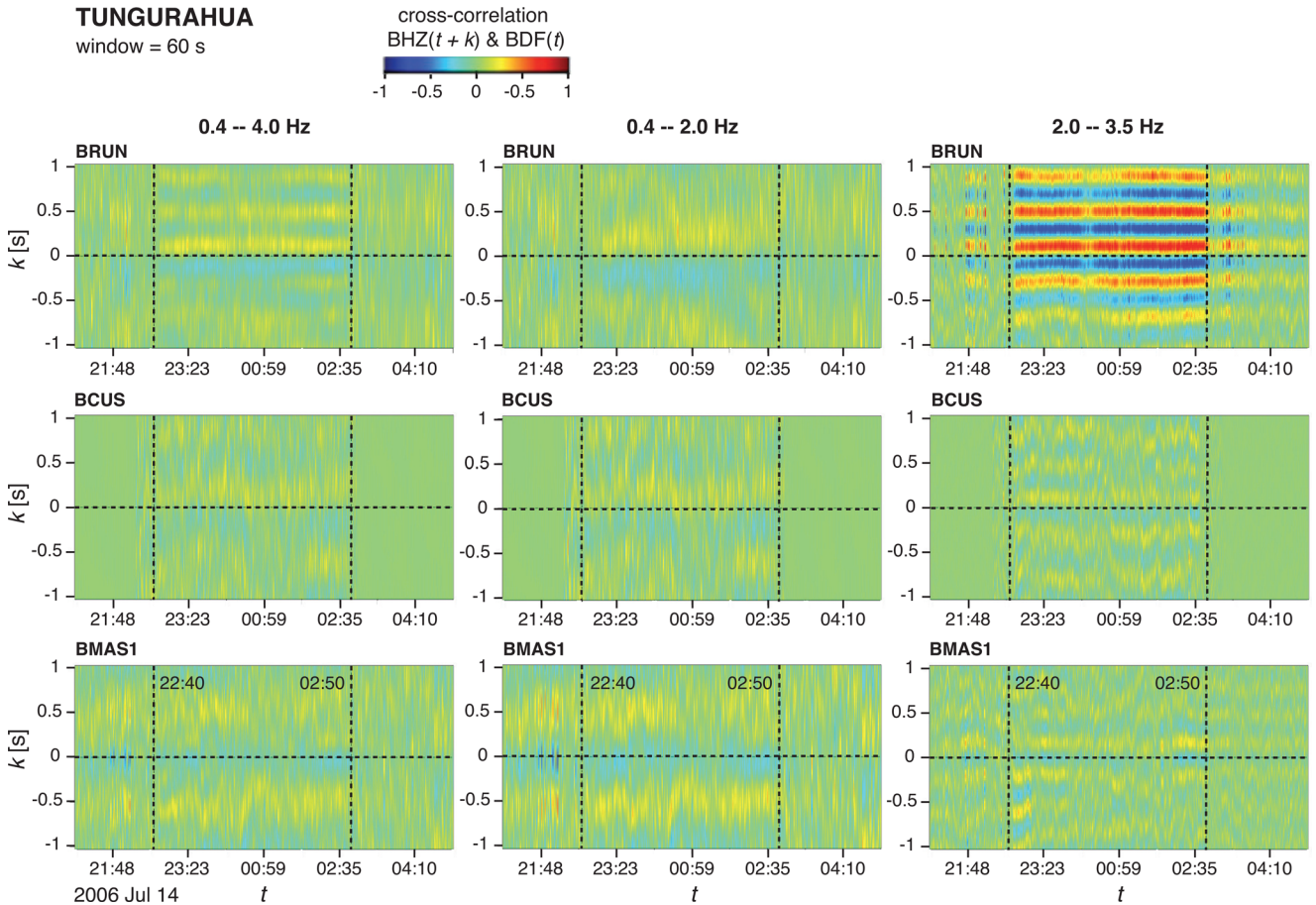
Figure 11. Cross-correlograms between vertical seismic component (BHZ) and infrasound component (BDF), at each station, of 2006 July 14 paroxysm, computed for three frequency bands, 0.4–4, 0.4–2 and 2–3.5 Hz. Vertical axes are the lag times k of the seismic component relative to the acoustic. Vertical dashed lines mark the initial (22:40) and final (02:50) eruption times. Non-overlapped 60 s windows were used.

due to backscattering and constructive interference of transmitted seismic waves.

6.4 Insights into the source type of paroxysmal eruptions

The correlation between seismic and acoustic records represented by nearly stable VASR values (Fig. 6) provides insights into the source types, which according to eq. (6) must be of the same type. Hence, the nine possible pairs of source types (combinations of three seismic with three acoustic possibilities) are now reduced to three, namely:

(i) Both seismic and acoustic sources are monopolar. Monopolar seismic waves are possible to be produced either by a spherical pulsating source (an isotropic radiator) or a source that is represented by the rate of increase of fluid volume per unit volume of the fluid, being generally time dependent (e.g. Howe 2003). In a first approximation, the seismicity and infrasound radiated by explosions can be modelled in this way. However a sustained eruptive column, the volcanic plume, cannot produce this type of acoustic source (Lighthill 1952). Because of the nature of our problem we discard this source type combination.

(ii) Both seismic and acoustic sources are dipolar. Pressure changes can be propagated due to forces acting on the fluid (the divergence of the force field is not null, Howe 2003). This occurs in the fluid-solid interaction. During a sustained eruption ejected solids interact with the atmosphere, or the ejected gases interact with the

conduit walls and the volcanic vent. Additionally, the fragmentation process creates a region of high pressure gradients affecting both the gas-pyroclast mixture and the volcanic edifice sector that confines the fragmentation region. This opens the possibility of modelling the transmitted seismic radiation with dipolar sources.

(iii) Both seismic and acoustic sources are quadrupolar. It is well known that jets, a fluid-fluid interaction, produces instabilities, which are modelled with quadrupolar sources (e.g. Lighthill 1952; Matoza *et al.* 2013). In solids, this type of radiation (double couple) also is observed in earthquakes that last less than our paroxysm and produce high frequency waves in the near field, which is not observed in our case. Therefore, we also discard this source type combination.

Thus, we suggest that the existence of a linear scaling between seismic and acoustic intensities is related to dipolar seismic and acoustic sources, which may be dominant in the near field. It is worthy to clarify two aspects. First, this hypothesis is not opposed to the presence of quadrupolar sources from the volcanic plume, it is just that their intensities are expected to be weaker than dipolar intensities. And second, in the near field spatial-distributed dipolar sources should be considered, therefore the radiation pattern can strongly differ from that originated by a single dipolar source. In any case, the mechanisms behind the linear correlation between seismic and acoustic records exposed in this work, could be further investigated within the theoretical framework of the acoustics of fluid-structure interaction (e.g. Howe 1998).
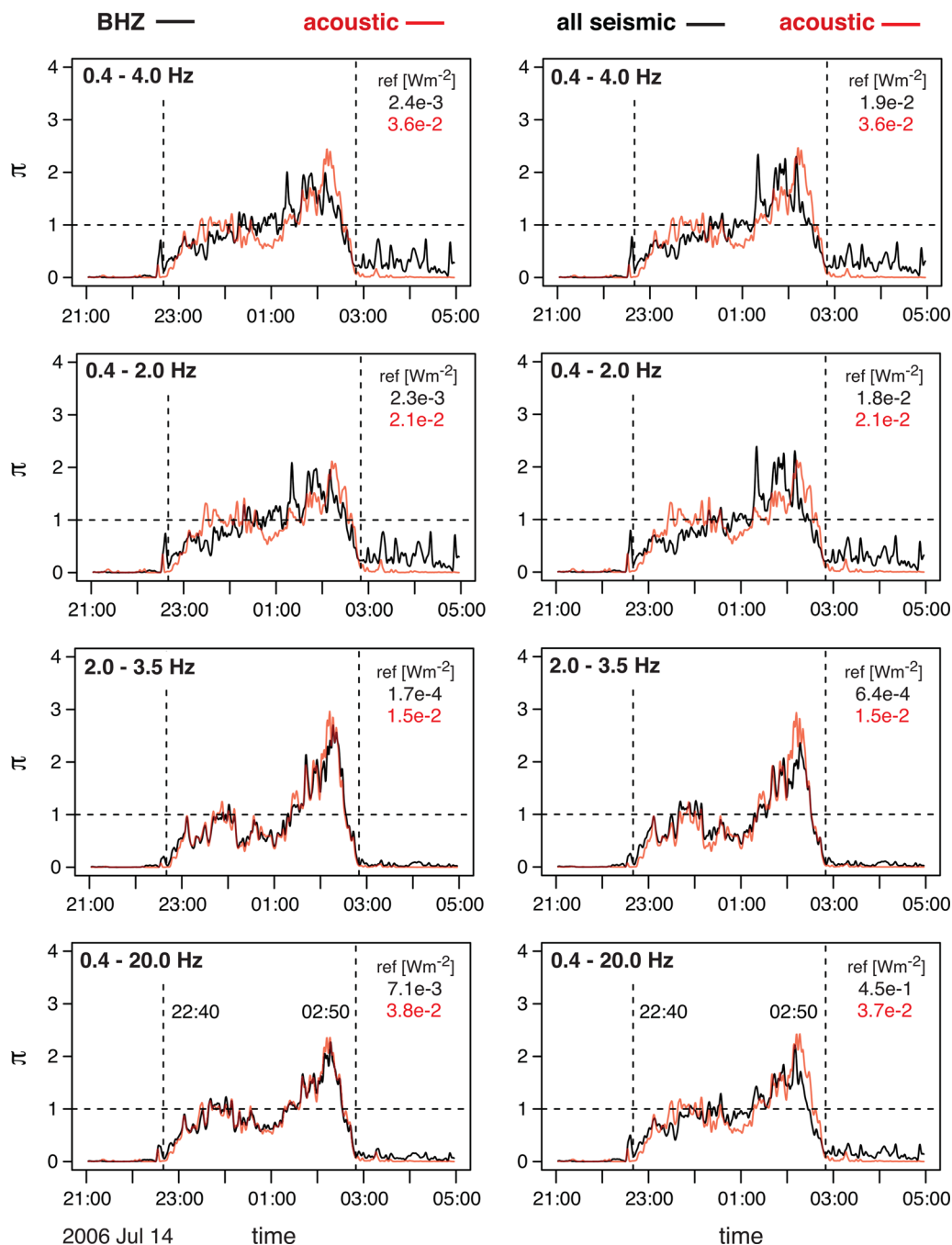
BRUN

Figure 12. Seismic (black) and acoustic (red) smoothed indices π at BRUN station from selected frequency ranges. Seismic indices computed only with the vertical component (left panels) and computed with all seismic components (right panels) are presented. Mean intensities (in W m^{-2}) used as reference levels (eq. 9) appear at the top-right corner of each panel. Indices at bottom panels are computed without site effect corrections. Vertical dashed lines mark the initial and final times of the eruption period.

6.5 VASR changes

VASR changes have been interpreted as differences in eruptive physical processes (e.g. Johnson & Aster 2005). If we quantify the VASR variability with the number of orders, in base 10, we obtain a parameter to compare different cases. Let ξ be this variability,

$$\xi = \log_{10}(\eta_{max}) - \log_{10}(\eta_{min}) = \log_{10}\left(\frac{\eta_{max}}{\eta_{min}}\right), \qquad (20)$$

where η_{max} and η_{min} are the upper and lower limits in eq. (14), respectively, which define the grey region of each station in Fig. 6. $\xi = 1$ represents one order of VASR variation. 2006 July 14–15 paroxysm presents variabilities $\xi = 0.77$ (BRUN), $\xi = 0.84$ (BCUS) and $\xi = 1$ (BMAS1). On the other hand, Johnson & Aster (2005), for instance, studying Karymsky and Erebus volcanoes present VASR values of explosions with variabilities between 1 and 3 orders. In this context, we observe that paroxysmal VASR

values of our case study are more stable than those observed in explosions.

VASR changes observed in paroxysms may be related to physical-temporal variations of the eruption. For instance, temperature of the ejected mixture and the amount of entrained mass may affect the acoustic radiation pattern. Location changes of the fragmentation region, with different geological properties, may affect recorded seismic intensities. These physical processes need further investigation.

7 CONCLUSIONS

We have found that the 2006 July 14–15 paroxysm of Tungurahua volcano has low frequency (0.4–4 Hz) seismic intensities linearly correlated with the acoustic intensities, with a coefficient of 0.60 and 0.56 at BRUN and BCUS, respectively. Such correlation indicates that the seismic and acoustic indices temporally vary in a similar manner, which implies that the corresponding sources are of the same type. Furthermore, because the eruption involves fluid-solid interactions, we conclude that the dipolar sources, likely distributed spatially, are dominant in our near field recordings. Similar correlations where found by Cannata *et al.* (2013) studying paroxysms of Etna volcano. They found correlations over 70–75 per cent between the root mean square (RMS) of amplitudes of seismic and acoustic records, within a similar seismic frequency range (0.5–5.5 Hz) to our case, and in the near field also. This suggests that our physical interpretation about the source type may be extended to other volcanoes. Here it is worthy to note that we have preferred to construct indices based on intensities, which are proportional to the energy releases, instead of based on RMS values, which is common in many observatories, because the paroxysmal intensity is a physical parameter that can be used for a direct interpretation of the hazard level.

The analysis of our data shows that the seismic-acoustic correlations at low frequency cannot be explained only by assuming wave couplings at the air-ground boundary. Therefore, a common origin is needed, namely the source of the eruptive process, which we argue is the pressure change in the fragmentation region and the consequent interaction of the ejecting mixture with the volcanic edifice. Such a source and its interactions might be considered as an extended distribution of dipoles that cannot be reduced to a point source in the near field. Consequently, seismic tremor locations of a paroxysm, using short windows and monopolar point sources with isotropic radiation, should be only considered as an approximation and as an intensity centre of an extended source (e.g. Sciotto *et al.* 2011). These locations will point close to the fragmentation region only if the fragmentation process is spatially limited and triggers seismic energy more efficiently than the coupling of the mixture with the conduit walls. This requires a further theoretical treatment.

We highlight that volcanic hazard assessment may be significantly improved using the computation of seismic and acoustic indices in real time, for both low and high frequencies. The correlation is due to either a common source or acoustic wave coupling. Either way the correlation requires disturbed atmosphere due to the eruptive process. However, not only the correlation is important. Weak signals should be related to weak emissions and strong ones likely accumulate enough energy to produce pyroclastic flows. Then, the indices can be used to compare several paroxysms, or one in course against other previously recorded.

In conclusion, our seismic and acoustic indices and their ratio (VASR) provide insights into eruption processes. Furthermore, they also provide useful monitoring parameters that could be used in early warning systems.

REFERENCES

Bustillos, J. & Samaniego, P., 2011. Volcán Tungurahua: Tamaño de las erupciones explosivas, *7mas. Jornadas de Ciencias de la Tierra,* Departamento de Geología, Escuela Politécnica Nacional, Spanish.

Cannata, A., Montalto, P. & Patane, D., 2013. Joint analysis of infrasound and seismic signals by cross wavelet transform: detection of Mt. Etna explosive activity, *Nat. Hazards Earth Syst. Sci.,* **13,** 1669–1677.

Cioni, R., Marianelli, P., Santacroce, R. & Sbrana, A., 2000. Plinian and subplinian eruptions, in *Encyclopedia of Volcanoes,* pp. 477–494, ed. Sigurdsson, H., Academic Press.

Curle, N., 1955. The influence of solid boundaries upon aerodynamic sound, *Proc. R. Soc. A,* **231,** 505–514.

Fee, D. & Matoza, R.S., 2013. An overview of volcano infrasound: from Hawaiian to Plinian, local to global, *J. Volcanol. Geotherm. Res.,* **249,** 123–139.

Fee, D., Garcés, M. & Steffke, A., 2010. Infrasound from Tungurahua volcano 2006–2008: Strombolian to Plinian eruptive activity, *J. Volcanol. Geotherm. Res.,* **193,** 67–81.

Garcés, M. *et al.*, 2008. Capturing the acoustic fingerprint of stratospheric ash injection, *EOS, Trans. Am. geophys. Un.,* **89,** 40, 377–379.

Hall, M.L., Robin, C., Beate, B., Mothes, P. & Monzier, M., 1999. Tungurahua volcano, Ecuador: structure, eruptive history and hazards, *J. Volcanol. Geotherm. Res.,* **91,** 1–21.

Hall, M.L., Steel, A.L., Mothes, P.A. & Ruiz, M.C., 2013. Pyroclastic density currents (PDC) of the 16–17 August 2006 eruptions of Tungurahua volcano, Ecuador: geophysical registry and characteristics, *J. Volcanol. Geotherm. Res.,* **265,** 78–93.

Howe, M.S., 1998. *Acoustic of Fluid-Structure Interactions,* Cambridge Univ. Press.

Howe, M.S., 2003. *Theory of Vortex Sound,* Cambridge Univ. Press.

Ichihara, M., Takeo, M., Oikawa, J. & Oshimato, T., 2012. Monitoring volcanic activity using correlation patterns between infrasound and ground motion, *Geophys. Res. Lett.,* **39,** doi:10.1029/2011GL050542.

IGEPN, (Quito-OVT), 2006a. Reporte Semanal: Volcán Tungurahua, semana del 10 al 16 de Julio de 2006, *Instituto Geofísico – Escuela Politécnica Nacional,* No. 28, Spanish.

IGEPN, (Quito-OVT), 2006b. Resumen mensual: Actividad del volcán Tungurahua – Julio de 2006, *Instituto Geofísico – Escuela Politécnica Nacional,* Spanish.

Jessop, D.E. & Jellinek, A.M., 2014. Effects of particle mixture and nozzle geometry on entrainment into volcanic jets, *Geophys. Res. Lett.,* **41,** 3858–3863.

Johnson, J.B. & Aster, R.C., 2005. Relative partitioning of acoustic and seismic energy during Strombolian eruptions, *J. Volcanol. Geotherm. Res.,* **148,** 334–354.

Kendall, M.G., 1969. Studies in history of probability and statistics, XXI. The early history of index numbers, *Rev. Int. Stat. Inst.,* **37**(1), 1–12.

Kerns, G. J., 2010, Introduction to Probability and Statistics Using R, ISBN: 978-0-557-24979-4, IPSUR R package at http://www.r-project.org/, last accessed 23 May 2015.

Kim, K., Lees, J.M. & Ruiz, M., 2012. Acoustic multipole source model for volcanic explosions and inversion for source parameters, *Geophys. J. Int.,* **191,** 1192–1204.

Kumagai, H. *et al.*, 2007. Enhancing Volcano-Monitoring Capabilities in Ecuador, *EOS, Trans. Am. geophys. Un.,* **88**(23), 245–252.

Kumagai, H., Palacios, P., Maeda, T., Barba, D. & Nakanu, M., 2009. Seismic tracking of lahars using tremor signals, *J. Volcanol. Geotherm. Res.,* **183,** 112–121.

Lacanna, G. & Ripepe, M., 2013. Influence of near-source volcano topography on the acoustic wavefield and implication for source modeling, *J. Volcanol. Geotherm. Res.,* **250,** 9–18.

Lele, S.K. & Nichols, J.W., 2014. A second golden age of aeroacoustics? *Phil. Trans. R. Soc. Lond., A.,* **372,** doi:10.1098/rsta.2013.0321.

Leys, C., Ley, C., Klein, O., Bernard, P. & Licata, L., 2013. Detecting outliers: do not use standard deviation around the mean, use absolute deviation around the median, *J. Exp. Soc. Psychol.,* **49,** 764–766.

Lighthill, M.J., 1952. On Sound Generated Aerodynamically. I. General Theory, *Proc. R. Soc. A,* **211,** 564–587.

Lighthill, M.J., 1954. On sound generated aerodynamically. I. Turbulence as a source of sound, *Proc. R. Soc. A,* **222,** 1–32.

Matoza, R.S. & Fee, D., 2014. Infrasonic component of volcano-seismic eruption tremor. *Geophys. Res. Lett.,* **41,** 1964–1970.

Matoza, R.S., Fee, D., Garcs, M.A., Seiner, J.M., Ramn, P.A. & Hedlin, M.A.H., 2009. Infrasonic jet noise from volcanic eruptions, *Geophys. Res. Lett.,* **36,** L08303, doi:10.1029/2008GL036486.

Matoza, R.S., Fee, D., Neilsen, T.B., Gee, K.L. & Ogden, D.E., 2013. Aeroacoustic's of volcanic jets: acoustic power estimation and jet velocity dependence, *J. geophys. Res.,* **118,** 6269–6284.

Newhall, C. & Self, S., 1982. The Volcanic Explosivity Index (VEI): an estimate of the explosive magnitude for historical volcanism, *J. geophys. Res.,* **87**(C2), 1231–1238.

Palacios, P., Kendall, J-M. & Mader, H., 2015. Site effect determination using seismic noise from Tungurahua volcano (Ecuador): implications for seismo-acoustic analysis, *Geophys. J. Int.,* **201,** 1082–1098.

R Core Team 2016. R: A language and environment for statistical computing. R Foundation for Statistical Computing, Vienna, Austria, available at: http://www.R-project.org/, last accessed 18 March 2016.

Sciotto, M., Cannata, A., Di Grazia, G., Gresta, S., Privitera, E. & Spina, L., 2011. Seismoacoustic investigations of paroxysmal activity at Mt. Etna volcano: new insights into the 16 November 2006 eruption, *J. geophys. Res.,* **116,** B09301, doi:10.1029/2010JB008138.

Shumway, H. & Stoffer, D., 2010. *Time Series Analysis and Its Applications,* 3rd edn, Springer.

Steffke, A.M., Fee, D., Garcés, M. & Harris, A., 2010. Eruption chronologies, plume heights and eruption styles at Tungurahua volcano: integrating remote sensing techniques and infrasound, *J. Volcanol. Geotherm. Res.,* **193,** 143–160.

Stein, S. & Wysession, M., 2003. *An Introduction to Seismology, Earthquakes, and Earth Structure,* Springer.

Suzuki, T., 2010. A review of diagnostic studies on jet-noise sources and generation mechanisms of subsonically convecting jets, *Fluid Dyn. Res.* **42,** 014001, doi:10.1088/0169-5983/42/1/014001.

Tam, C.K.W., 1998. Jet noise: since 1952, *Theor. Comput. Fluid Dyn.,* **10,** 393–405.

Tam, C.K.W., Viswanathan, K., Ahuha, K.K. & Panda, J., 2008. The sources of jet noise: experimental evidence, *J. Fluid Mech.,* **615,** 253–292.

Troncoso, L., Le Pennec, J.-L., Jaya, D., Valle, A., Mothes, P. & Arrais, S., 2006. Depósitos de caída de ceniza producidos durante las erupciones del volcán Tungurahua, 14 de julio y 16 de agosto de 2006, *6tas. Jornadas de Ciencias de la Tierra, Departamento de Geología, Escuela Politécnica Nacional,* 181–184, Spanish.

Viswanathan, K., 2011. Alteration of jet noise by jet plume deflection, *AIAA J.,* **49**(1), 250–253.

Viswanathan, K. & Czech, M.J., 2009. Role of jet temperature in correlating jet noise, *AIAA J.,* **47**(1), 1090–1106.

Woods, A.W., 2010. Turbulent plumes in nature, *Annu. Rev. Fluid Mech.,* **42,** 391–412.

Woulff, G. & McGetchin, T.R., 1976. Acoustic noise from volcanoes: theory and experiment, *Geophys. J. R. astr. Soc.,* **45,** 601–616.

Yokoo, A. & Suzuki Y.J. & Iguchi, M., 2014. Dual Infrasound sources from a vulcanian eruption of sakurajima volcano inferred from cross-array observation, *Seismol. Res. Lett.,* **85**(6), 1212–1222.

APPENDIX: EXAMPLE OF OUTLIER DETECTION

In this appendix we describe the procedure to identify outliers within a time-series of positive values, using both the whole signal and its high-frequency components, applying to an example of synthetic data. We start constructing the stationary time-series:

$$z_t = 0.9z_{t-1} + \beta_t(5,5), \quad t > 2, \quad z_1 = 5, \tag{A1}$$

where β_t are Beta distribution random variables, which take values between 0 and 1 (Kerns 2010). They have two shape parameters whose values are equal to 5 for this example, which generates symmetric distributions centred at 0.5. Fig. A1(a) shows the first 1000 points of this time-series that can be reproduced in R (R core team 2016) using the instruction set.seed(1). Three outliers below the lower threshold of eq. (14), represented with solid red dots, appear. Fig. A1(b) shows the filtered time-series with its respective threshold given by eq. (15) and two additional outliers appearing, where a zero-shift high pass filter from 0.1 cps (cycles per sampling time interval) has been used. Nyquist's frequency is 0.5.

Then, we disturb the time-series z_t adding 20 intrusive values at $t = 25, 75, 125, \ldots, 925, 975$, with values of the sequence $-1, 1, -1, 1, \ldots, -1, 1$. They do not follow eq. (A1) and cause the appearance of some spikes (Fig. A1c), each one representing a rupture of the background time-series z_t. After using eq. (14), half of them are not detected (open red dots). In order to detect them, two steps are needed. First, all outliers values that were found using eq. (14) are replaced by interpolated data. This step is important because very large outliers can cause large distortions in filtered time-series. Second, the power spectrum of this modified time-series is computed (Fig. A1f) to look for the frequency range, associated to low frequencies, that includes the major percentage of power. In this example, we found that 80 per cent of the power is below 0.096 cps. Fig. A1(d) shows the outliers after using the high pass filter over 0.1 cps, where all intrusive values were detected. Finally, Fig. A1(e) reproduces the original time-series with the detected outliers. The process has identified all outliers from the simulated time-series plus the twenty added spikes.

Additionally, note that if several consecutive outliers are not identified by eq. (14), the method of using high-frequency components may fail. For instance, if the outliers have similar values, the high pass filter could not detect them. Cases like this require a further analysis.
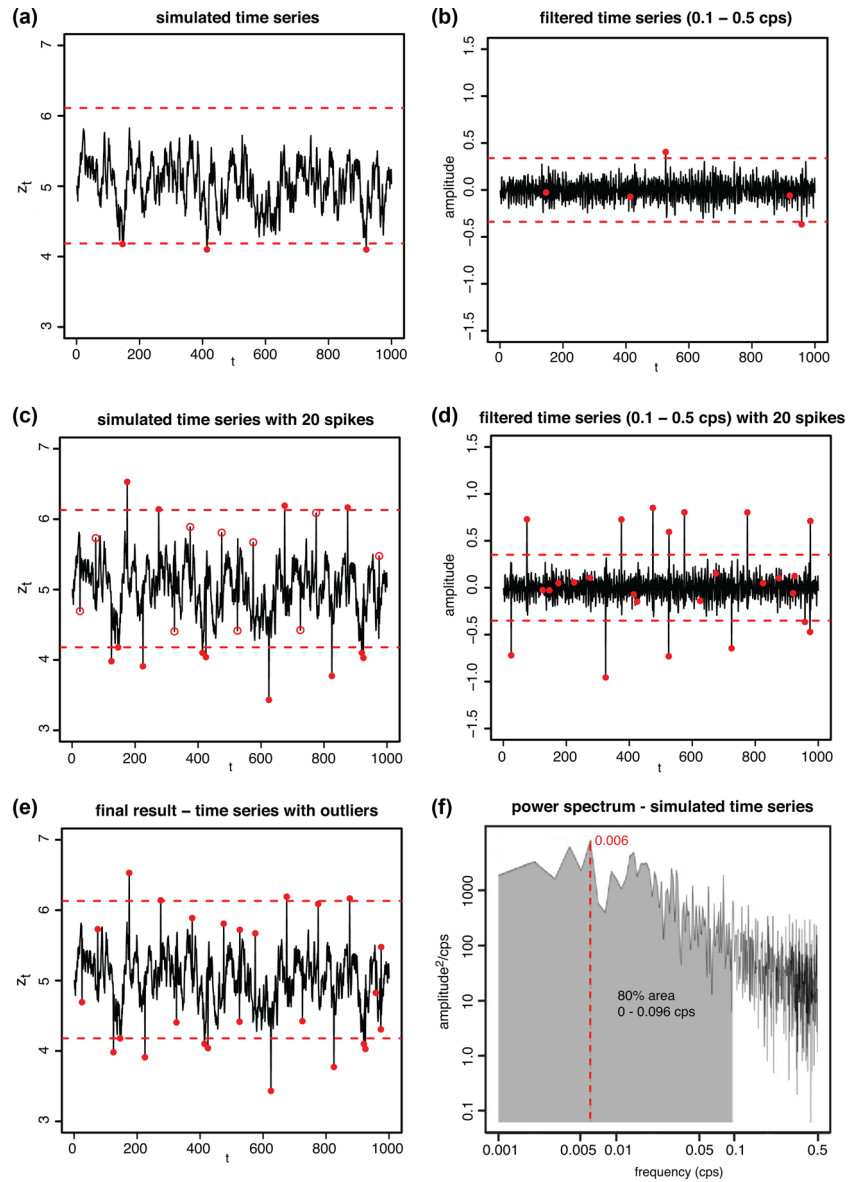
Figure A1. (a) Simulated time-series, eq. (A1), with lower and upper limits (red dashed lines) and three outliers detected (solid red dots). (b) Time-series filtered between 0.1 and 0.5 cps after replacing outliers of panel (a) with interpolated values. Two additional outliers appear. (c) Time-series given in panel (a) after adding 20 intrusive values. Solid red dots are detected outliers and open red dots are non-detected outliers. (d) Filtered time-series between 0.1 and 0.5 cps, after replacing outliers of panel (c) with interpolated values. (e) Time-series with identified outliers in panels (c) and (d). (f) Power spectrum of simulated time-series, after removing its trend and replacing outliers in panel (c) with interpolated values. The grey region (0–0.096 cps) includes 80 per cent of the total power around the peak frequency (0.006 cps).